Cross sections for electron excitation of the $2\,^3S$ metastable level of He into higher triplet levels

Garrett A. Piech, Mark E. Lagus, L. W. Anderson, and Chun C. Lin
Department of Physics, University of Wisconsin, Madison, Wisconsin 53706

M. R. Flannery
School of Physics, Georgia Institute of Technology, Atlanta, Georgia 30332

(Received 25 September 1996)

Cross sections for electron excitation out of the $2\,^3S$ metastable level of He into the $2\,^3P$, $3\,^3S$, $3\,^3P$, $3\,^3D$, $4\,^3S$, $4\,^3P$, $4\,^3D$, $5\,^3S$, and $5\,^3D$ levels have been obtained for energies up to 18 eV. We have observed a broad excitation function for the $2\,^3P$ level with a peak apparent cross section of 1.2×10^{-14} cm^2. For the $n=3$, 4, and 5 levels, the excitation functions show a pattern of sharp peaks for excitation into the $n\,^3S$ levels, slightly less sharp peaks for excitation into the $n\,^3P$ levels, and relatively broad peaks for excitation into the $n\,^3D$ levels. Absolute cross sections have been obtained for all the above mentioned levels using a laser-induced fluorescence technique and the results agree well with experimental values reported by Lagus *et al.* [Phys. Rev. A **53**, 1505 (1996)] The cross sections for the $2\,^3S\rightarrow n\,^3P$ excitations which correspond to dipole-allowed optical transitions are smaller than the corresponding $2\,^3S\rightarrow n\,^3S$ and $2\,^3S\rightarrow n\,^3D$ excitation cross sections, in contrast to the trends observed for excitations out of the ground level. This reversal behavior is discussed in terms of the dipole matrix element sum rule. Our cross-section data are compared with those of the alkali-metal atoms. [S1050-2947(97)06204-5]

PACS number(s): 34.80.Dp

I. INTRODUCTION

Excitation out of the metastable levels of rare gases is an important mechanism in a wide variety of phenomena, such as high density gas discharges, astrophysical plasmas, and electron-beam pumped lasers. In the case of the $2\,^1S$ and $2\,^3S$ metastable levels of helium, much theoretical work has been done on calculating both differential and integral cross sections for electron excitation out of these excited levels [1–7]. An early measurement by Gostev *et al.* [8] shows results that are in serious disagreement with the subsequent experiment of Mityureva and Penkin [9]. Measuring cross sections for processes out of the metastable levels has proven to be much more difficult than measuring cross sections for the corresponding processes out of the ground levels of these gases. This is primarily due to the difficulty in producing sufficient densities of metastable atoms to study and separating the associated signal from signals due to ground level atoms. In our laboratory we have used a hollow cathode discharge to produce a thermal atomic beam containing metastable helium with a density of 6×10^7 cm^{-3}. With this apparatus, along with the use of special techniques for detecting very low photon emission signals, we have measured excitation functions and cross sections for electron excitation out of both the singlet and triplet metastable levels for electron energies up to the onset of ground level excitation [10–12]. Our current work represents a refinement and extension into the $n=2$ and $n=5$ triplet levels of the previous results of Rall *et al.* [10]. We have found distinct patterns in the shapes of the excitation functions for the S, P, and D levels.

Part of the motivation for our effort is that the experiment of Rall *et al.*, which used the aforementioned thermal atomic beam as a target, and the experiment of Lagus *et al.* [13], which used a fast (1 keV) beam of metastable atoms produced by charge exchange collisions as a target, had a difference in their absolute cross sections of about 50%. We feel that it is important to improve the absolute calibration of the thermal atomic beam experiment to determine the source of this discrepancy. As discussed in Sec. III E, with the improved absolute calibration our absolute cross-section measurements using the thermal metastable beam target show good agreement with the results of Lagus *et al.*, which are based on an entirely different method of absolute calibration.

II. EXPERIMENTAL APPARATUS

A schematic diagram of our experimental apparatus is shown in Fig. 1, which is quite similar to the apparatus described by Lockwood *et al.* [11,12]. In this experiment, an electron-beam crosses at right angles an atomic beam containing both ground-state and metastable He atoms produced by a hollow cathode discharge. The emission intensity from

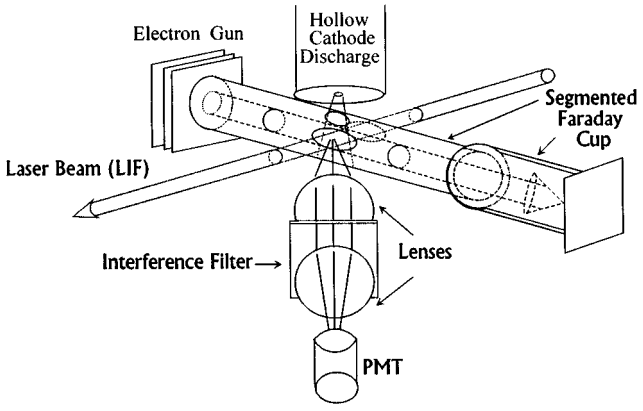

FIG. 1. Schematic diagram of the experimental apparatus used.

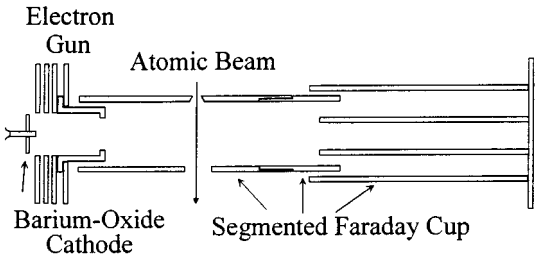

FIG. 2. Schematic diagram of electron gun and segmented Faraday cup used in the experiment.

the He($n\,^3L$) atoms produced by electron-impact excitation is measured to determine the cross sections. The electron beam is kept below 19 eV so that only the metastables are excited, and the resulting fluorescence is detected by a photomultiplier tube (PMT). Ultrahigh purity He (99.9999%) is used in the hollow cathode discharge. A high voltage, constant-current power supply is used to operate the discharge and is typically run at 100 mA and 600 V. The helium pressure inside the discharge is roughly 7 torr. When the discharge is first started after cleaning the apparatus, it typically takes a day or two for the discharge to ''settle'' to these voltage and current levels, after which it generally runs stably for a period of many weeks. The atoms from the discharge effuse into the collision region through a 1 mm diameter hole at the bottom of the discharge. The emerging atomic beam consists of both $2\,^1S$ and $2\,^3S$ metastable He atoms, and ground state ($1\,^1S$) He atoms. Laser-induced fluorescence (LIF) of the atomic beam, as described in Sec. III, has shown that it consists of approximately 3×10^{-7} metastables per ground-state He atom, of which about 17% of the metastable atoms are in the $2\,^1S$ level and 83% are in the $2\,^3S$ level. This gives a metastable number density of 6×10^7 cm^{-3} in the collision region. The metastable number density, as well as the singlet to triplet ratio, depends on the discharge conditions.

Electron excitation into the $n\,^3L$ levels will be due to excitation out of both metastable levels, but since we have predominantly $2\,^3S$ metastables, and since spin conserving $2\,^3S\rightarrow n\,^3L$ excitation is much more favorable than spin changing $2\,^1S\rightarrow n\,^3L$ excitation, we can attribute our observed fluorescence signals almost entirely to excitation out of the $2\,^3S$ level. However, in Sec. IV A we do describe our observation of a small amount of $2\,^1S\rightarrow n\,^3L$ excitation which manifests itself as small shoulders in our excitation functions.

A modulated electron beam is produced by an indirectly heated barium-oxide cathode mounted in a triode configuration electron gun. All voltages in the electron gun are kept below 19 V. Since the energy of the lowest excited level (the $2\,^3S$) in He is 19.8 eV, this ensures that no excitation of ground-state atoms occurs within the gun. Helmholtz coils produce a magnetic field (coaxial to the electron beam) of approximately 10 Gauss in order to collimate the electron beam. A typical electron current produced by this gun is 10 μA at 10 eV. The electron-beam current is measured by a segmented Faraday cup [12] shown in Fig. 2. All parts of the Faraday cup and the electron gun are thoroughly blackened using goldblack, in order to minimize scattered light from both the electron gun cathode and from the discharge. This greatly reduces the background light seen by the PMT and significantly improves the statistics of the experiment.

The light from the excitations is collected by a quartz (f/1.3) lens located 1 focal length from the collision region. The viewing direction is on a plane perpendicular to the atomic beam and makes a 60° angle with the electron beam as illustrated in Fig. 1. The collimated light is then sent through a narrow bandpass filter [10 Å full width at half maximum (FWHM)] selected for the transition of interest. A second identical quartz lens focuses the filtered light onto the photocathode of a photomultiplier tube (either an S-20 or S-1 photocathode). The amplified pulses from the photomultiplier tube are fed into two counters: an A counter operating when the electron beam is on, and a B counter operating when the electron beam is modulated off. This modulation of the electron beam enables us to subtract off the large amount of background light emitted by the discharge and electron gun cathode. The difference of the two counters (A-B) is then divided by the electron current collected by the Faraday cup to obtain a relative signal at a given beam energy. A typical background (B) count rate is 7000 counts/sec, with a signal (A-B) count rate of 300 counts/sec. With this experiment excitation functions out of the metastable levels can only be obtained for electron energies less than the onset for excitation out of the ground state. Above ground-state onset, signal from excitations out of the ground state dominates due to the preponderance of ground-state atoms in the atomic beam ($\sim10^7$ ground-state atoms per metastable).

Since the experiment is performed at low electron energies, and since the voltages on the electron gun must be kept low in order to prevent ground-state excitation within the gun itself, it is difficult to ensure that the electron beam is well collimated at all energies of interest. We have also noted that the atomic beam can significantly scatter our electron beam. Thus a careful check must be made to ensure that no artifacts are introduced into the shapes of the excitation functions due to spreading of the electron beam. This is done by introducing a small amount of solid Na into the hollow cathode discharge, which gets sputtered into the atomic beam by the energetic helium atoms. We monitor the excitation function of the Na 589 nm ($3\,^2P\rightarrow3\,^2S$) emission, and compare the shape of our observed excitation function to that of the known 589 nm optical emission excitation function [14]. When this experiment is performed, our excitation function closely matches the known Na curve as long as we have a collimating magnetic field of 10 Gauss.

We have made a number of modifications to the experiment since the publication of Ref. [10]. We now run the hollow cathode discharge at twice the He pressure of Rall *et al.* This increases the number of metastables in the atomic beam, and thus gives greater signal. Special attention has been given to making sure that the parts near the collision region are completely covered by goldblacking. The integrity of the goldblacking is checked periodically to make sure that it has not been damaged. This greatly reduces scattered light. These improvements help us to enhance the signal to noise ratio of our excitation functions out of the $2\,^3S$ level by a factor of 10 or more over the results of Rall *et al.* We have also made use of an S-1 photocathode in order to obtain the $2\,^3P$ excitation function by observing the infrared (1.0829 μm) $2\,^3P\rightarrow2\,^3S$ transition.

III. ABSOLUTE CALIBRATION

In our experiment we determine the $2\,^3S$ metastable target density by passing a laser beam tuned to the $2\,^3S \rightarrow 3\,^3P$ absorption frequency and measuring the laser-induced fluorescence (LIF) of the $3\,^3P \rightarrow 2\,^3S$ emission. The LIF intensity emitted, along with the known $2\,^3S \rightarrow 3\,^3P$ oscillator strength, gives the $2\,^3S$ metastable density, enabling absolute measurement of cross sections for excitation out of the $2\,^3S$ metastable level. The same principle for absolute calibration was previously utilized by Rall *et al.* [10]. In an independent experiment Lagus *et al.* have used a fast (~1 keV) metastable atomic beam to measure electron excitation cross section out of the $2\,^3S$ level into the $3\,^3S$, $3\,^3P$, $3\,^3D$, and $4\,^3D$ levels. They absolutely calibrate their experiment in a manner entirely different from the LIF method. The results of Rall *et al.* are about 50% higher than the results obtained by Lagus *et al.* in the fast beam metastable experiment. In order to resolve this discrepancy, we have performed a new absolute calibration of this experiment, which differs from the procedure used in Refs. [10–12] in two regards. We have used a cw laser to perform our LIF measurement, in contrast to the use of a pulsed dye laser by Rall *et al.* We have also taken advantage of our improved signal to noise ratio to examine the effects of the nonuniformity of the electron and atomic beams on the absolute cross-section results, which we were unable to do in the earlier experiments.

A. Method

In general, one can express the number of excitations observed per volume per second that occur when an electron beam is sent through a target gas as the product of the detection efficiency (η) times the electron-beam flux (J/e) times the cross section (Q) times the target density (n)

$$\frac{(\text{excitations observed})}{(\text{volume}\times\text{sec})} = \eta\left(\frac{J}{e}\right)Qn. \tag{1}$$

Thus in order to extract cross sections from a ''signal'' measured in an electron excitation experiment such as this, one needs to know, in absolute terms, three things: the metastable target density, the optical and electronic collection efficiency of the apparatus used, and the current density of the electron beam. The general technique we use is as follows. Using the LIF technique mentioned above, we ratio the metastable electron excitation signal to the LIF signal, for which the optical absorption cross section is known, to determine our metastable density. We also ratio the metastable electron excitation signal to the signal for electron excitation out of the ground level (for which the electron excitation cross section is known) to eliminate the need to know the optical and electrical efficiencies of our apparatus. We directly measure the electron-beam current using a Faraday cup.

If the number density and the electron beam are not spatially uniform, then Eq. (1) must be written in integral form. In addition, the detection efficiency of the optics may be spatially nonuniform. We can then write

$$\frac{(\text{excitations observed})}{(\text{volume}\times\text{sec})} = \xi Q \int \Omega(\vec{r})[J(\vec{r})/e]n(\vec{r})d^3\vec{r}, \tag{2}$$

where we have split the detection efficiency into two parts, ξ for the electronic detection efficiency, and $\Omega(\vec{r})$, representing the probability of collecting a photon as a function of the position of the emitting atom. For our experiment we can thus write two equations, one describing the (A-B) photon counts obtained when we perform electron excitation out of the $2\,^3S$ metastable level into the $3\,^3P$ level (at 10 eV), and another equation for the (A-B) photon counts observed when we perform excitation out of the $1\,^1S$ ground level into the $3\,^3P$ level (at the energy corresponding to the peak of the ground-state excitation function),

$$(A\text{-}B)^{3\,^3P}_{\text{meta}}(10\ \text{eV}) = \xi_{3\,^3P\rightarrow 2\,^3S} Q^{3\,^3P}_{\text{meta}}(10\ \text{eV})\beta_{3\,^3P\rightarrow 2\,^3S} \times \int \Omega(\vec{r}) n_{2\,^3S}(\vec{r})[J^{10\ \text{eV}}(\vec{r})/e]d^3\vec{r}, \tag{3}$$

$$(A\text{-}B)^{3\,^3P}_{\text{gs}}(\text{peak}) = \xi_{3\,^3P\rightarrow 2\,^3S} Q^{3\,^3P}_{\text{gs}}(\text{peak})\beta_{3\,^3P\rightarrow 2\,^3S} \times \int \Omega(\vec{r}) n_{\text{gs}}(\vec{r})[J^{\text{peak}}(\vec{r})/e]d^3\vec{r}. \tag{4}$$

Here $Q^{3\,^3P}_{\text{meta}}$ (10 eV) and $Q^{3\,^3P}_{\text{gs}}$ (peak) are the apparent cross sections for excitation into the $3\,^3P$ level out of the metastable level (at 10 eV) and out of the ground level (at the peak of the ground-state excitation function), respectively. $J^{10\ \text{eV}}(\vec{r})$ and $J^{\text{peak}}(\vec{r})$ are the electron current densities at those two energies, $n_{2\,^3S}(\vec{r})$ and $n_{\text{gs}}(\vec{r})$ are the number densities of the metastable and ground level atoms in the collision region, $\xi_{3\,^3P\rightarrow 2\,^3S}$ is the electronic detection efficiency for the $3\,^3P \rightarrow 2\,^3S$ transition, and $\beta_{3\,^3P\rightarrow 2\,^3S}$ is the branching ratio. The photon counting signals for both excitation processes are obtained using exactly the same optics and data collection system, so that the electronic efficiency $\xi_{3\,^3P\rightarrow 2\,^3S}$ is the same as in Eqs. (3) and (4), and the same is true for the optical collection efficiency, $\Omega(\vec{r})$. The metastable excitation functions are calibrated at 10 eV since this energy is typically past any rapidly changing portion of the excitation function and any contribution from spin-changing excitations ($2\,^1S \rightarrow n\,^3L$) should be small at this energy [12].

One can also write a similar equation for the *analog* signals due to ground-state electron excitation and laser-induced fluorescence of the $2\,^3S \rightarrow 3\,^3P$ transition

$$S_{\text{gs}}(\text{peak}) = \chi_{3\,^3P\rightarrow 2\,^3S} Q^{3\,^3P}_{\text{gs}} \beta_{3\,^3P\rightarrow 2\,^3S} \int \Omega(\vec{r}) n_{\text{gs}}(\vec{r}) \times [J^{\text{peak}}(\vec{r})/e]d^3\vec{r}, \tag{5}$$

$$\int S_{\text{LIF}}(\nu_L)d\nu_L = \chi_{3\,^3P\rightarrow 2\,^3S}\beta_{3\,^3P\rightarrow 2\,^3S} \int \Omega(\vec{r}) n_{2^3S}(\vec{r}) \times \left\{ \int\int \sigma(\nu-\nu_0)[w(\nu_L;\vec{r})/h\nu_L] \times D(\nu-\nu_L)d\nu d\nu_L \right\} d^3\vec{r}. \tag{6}$$

Here $\int S_{\text{LIF}}(\nu_L)d\nu_L$ is the *integrated* LIF signal obtained as the laser frequency ν_L is scanned across the transition. $\chi_{3\,^3P\rightarrow 2\,^3S}$ is the electronic efficiency using the analog sys-

tem, $\sigma(\nu-\nu_0)$ is the optical absorption cross section at the frequency ν for the $2\,^3S\rightarrow 3\,^3P$ transition (resonant at frequency ν_0), $D(\nu-\nu_L)$ is the normalized frequency distribution of the laser power, and $w(\nu_L;\vec{r})$ is the laser power at the set frequency. Since $S_{\rm LIF}(\nu_L)$ is a sharply peaked function centered at $\nu_L=\nu_0$, the major contribution to the integrals in Eq. (6) comes from a small range of ν_L near ν_0. Within this range we can separate $w(\nu_L;\vec{r})$ into spatial and frequency components

$$w(\nu_L;\vec{r})=w(\nu_L)w_0(\vec{r}), \tag{7}$$

$$\int w_0(\vec{r})d^3\vec{r}=1, \tag{8}$$

where we have defined $w_0(\vec{r})$ as the normalized laser power spatial distribution. Furthermore, we can pull $[w(\nu_L)/h\nu_L]$ out of the integral and assign it the constant value $[w(\nu_0)/h\nu_0]$ so that

$$\int S_{\rm LIF}(\nu_L)d\nu_L=\chi_{3\,^3P\rightarrow 2\,^3S}\beta_{3\,^3P\rightarrow 2\,^3S}[w(\nu_0)/h\nu_0]\times\int\Omega(\vec{r})n_{2^3S}(\vec{r})w_0(\vec{r})\times\left[\int\int\sigma(\nu-\nu_0)D(\nu-\nu_L)d\nu d\nu_L\right]d^3\vec{r}. \tag{9}$$

Using the fact that the laser line shape is normalized, and the definition of oscillator strength for this transition,

$$\int D(\nu-\nu_L)d\nu_L=1, \tag{10}$$

$$f_{3\,^3P\rightarrow 2\,^3S}=(1/\pi r_0 c)\int\sigma(\nu-\nu_0)d\nu, \tag{11}$$

and integrating over the frequencies ν and ν_L, Eq. (9) can be rewritten as

$$\int S_{\rm LIF}(\nu_L)d\nu_L=\chi_{3\,^3P\rightarrow 2\,^3S}\beta_{3\,^3P\rightarrow 2\,^3S}(\pi r_0 c f_{3\,^3P\rightarrow 2\,^3S})\times[w(\nu_0)/h\nu_0]\int\Omega(\vec{r})n_{2^3S}(\vec{r})w_0(\vec{r})d^3\vec{r}. \tag{12}$$

Here r_0 is the classical radius of the electron, c is the speed of light, and $f_{3\,^3P\rightarrow 2\,^3S}$ is the oscillator strength as defined in Eq. (11). Using Eqs. (3), (4), (5), and (12), we can obtain an expression for the electron excitation cross section out of the $2\,^3S$ metastable level into the $3\,^3P$ level in terms of known and directly measurable quantities

$$Q^{3\,^3P}_{\rm meta}(10\ {\rm eV})=\left[\frac{(A\text{-}B)^{3\,^3P}_{\rm meta}(10\ {\rm eV})/I^{10\ {\rm eV}}}{(A\text{-}B)^{3\,^3P}_{\rm gs}({\rm peak})/I^{\rm peak}}\right]\left[\frac{S_{\rm gs}({\rm peak})}{I^{\rm peak}}\right]\times\left[\frac{\int S_{\rm LIF}(\nu_L)d\nu_L}{w(\nu_0)}\right]^{-1}\left[\frac{\pi r_e c f_{2\,^3S\rightarrow 3\,^3P}e}{h\nu_0}\right]\times\left[\frac{\int\Omega(\vec{r})n_{2^3S}(\vec{r})w_0(\vec{r})d^3\vec{r}}{\int\Omega(\vec{r})n_{2\,^3S}(\vec{r})J_0^{10\ {\rm eV}}(\vec{r})d^3\vec{r}}\right], \tag{13}$$

$$I^{\rm peak}=\int J^{\rm peak}(\vec{r})d^3\vec{r}, \tag{14}$$

$$I^{10\ {\rm eV}}=\int J^{10\ {\rm eV}}(\vec{r})d^3\vec{r}=I^{10\ {\rm eV}}\int J_0^{10\ {\rm eV}}(\vec{r})d^3\vec{r}. \tag{15}$$

We note that $w_0(\vec{r})$ and $J_0^{10\ {\rm eV}}(\vec{r})$ are normalized functions for the laser and electron-beam spatial distributions, so we can take the absolute magnitudes of the laser power and electron current out of the integrands for convenience. We note that Eq. (13) is independent of the ground-state cross section used in Eqs. (4) and (5). The terms in the first bracket of Eq. (13) are experimentally measurable quantities obtained when we measure our photon counting signals for excitation into the $3\,^3P$ out of the metastable level and out of the ground level. The terms in the second and third brackets are measured during the LIF calibration procedure as described in Sec. IV. The terms in the fourth bracket are all known constants. The terms in the final bracket are the beam overlap integrals, and they are described in more detail in the Sec. III C of this paper.

B. The LIF apparatus

To generate the necessary light for the LIF calibration, we used a Ti:Sapphire laser pumped by a 9 W Ar^+ laser to produce a bright beam at 7778 Å, and then used an angle-tuned $LiIO_3$ crystal to double the beam frequency, producing light at 3889 Å. A schematic of the entire apparatus is shown in Fig. 3. A lens focuses the approximately 800 mW Ti:Sapphire beam onto the $LiIO_3$ crystal, and the emerging beam, containing both the fundamental (7778 Å) and doubled (3889 Å) light, strikes a mirror and is sent towards the vacuum chamber. The intense fundamental light, and any other stray light collinear to the laser beam, is filtered out using the two interference filters shown, the first filter being a Corning colored glass filter, and the second filter is a 100 Å FWHM filter centered at 3900 Å. Two lenses collimate the laser beam and create an adjustable spot size at the main chamber. A chopper wheel operating at 170 Hz chops the beam on and off before it enters the main chamber. A typical cw (3889 Å) beam power achieved in the experiment, at the main chamber, is 1.5–2 μW. The same photomultiplier tube, interference filter, and optics that are used in recording the photon counting excitation functions are used to observe the fluorescence signal caused by the laser beam exciting the metastable beam. The reference signal from the chopper wheel and the output voltage from an electrometer, which

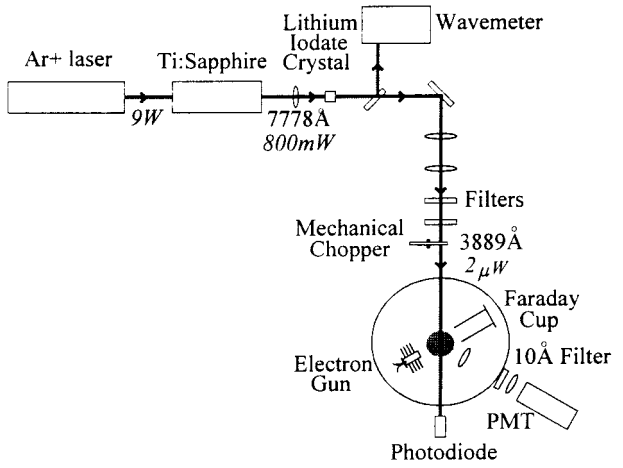

FIG. 3. Experimental setup for laser-induced fluorescence (LIF) calibration of the experiment.

reads the photomultiplier tube current, are fed into a lock-in amplifier. The output signal of the lock-in amplifier is recorded by a computer. The laser entrance and exit ports on the chamber are both Brewster windows oriented to give minimum reflection for the vertically polarized 3889 Å beam. On the far side of the chamber the laser-beam power is continuously monitored using a photodiode.

In order to obtain the integrated LIF signal $[\int S_{\mathrm{LIF}}(v_L)dv_L]$, we scan the Ti:Sapphire laser by tilting its birefringent filter stack with a stepping motor. This scans the fundamental beam frequency at a known rate (approximate 0.30 GHz/sec), and thus also scans the doubled-beam frequency at twice that rate. The laser frequency, and thus the scan rate, is recorded using a model WA-1500 wave meter from Burleigh Instruments. Once a scan is performed, we numerically integrate the resulting fluorescence curve with the computer. We determined the scattered light contribution to the observed signal by tuning the laser slightly off resonance, so that no LIF signal was present. When the laser beam was properly aligned, the contribution of the scattered light signal was small ($<5\%$) when compared to the LIF signal, and this small constant background was subtracted from our integrated fluorescence signal. As was previously mentioned, we also record a ground-state excitation signal by chopping the electron beam at 170 Hz, and recording the ground-state excitation signal at its peak with the detection system unchanged. This ensures that all optical or electronic collection efficiencies of the ground-state excitation and laser excitation are identical, and thus that the efficiency factors cancel.

C. The beam profiles

In order to calculate the last bracketed term in Eq. (13), we have to obtain information on the optical profile of our apparatus, and on the three beams involved in the experiment—the laser, electron, and metastable beams. To measure the optical profile $\Omega(\vec{r})$ (optical collection efficiency as a function of the position from which a photon is emitted) of our apparatus, we translated a point source of light across the collision region. The point source consisted of a hollow 3/16″ diameter aluminum tube with a 0.33 mm diameter hole drilled in its side. An optical fiber inserted into the tube provided the light source. The aluminum tube was mounted on a translation stage and the PMT signal was recorded as the tube was translated through the collision region of the experiment. The result was a nearly Gaussian optical profile with a FWHM of 4.0 mm.

In order to obtain the metastable number density $n_{2\,^3S}(\vec{r})$ as a function of position, we used a small diameter ($\sim$0.5 mm) laser beam to measure the LIF signal as we varied the location of the beam. The resulting LIF signals gave us a rough measure of the metastable density at different locations. We varied the location of the laser beam both horizontally and vertically. We have determined that the metastable density decreases by less than 5% for measurements made up to a position of ± 2 mm from the beam axis at a distance below the aperture of $z=13$ mm. The metastable density falls off as $1/z^2$ in the vertical direction. These measurements are consistent with the metastable atoms emerging from a nearly point source (the small aperture in the hollow cathode) with a $\cos\theta$ distribution, where θ is the angle made with respect to the beam axis.

In the previous calibration of Refs. [10–12], it was assumed that the laser and electron beams had nearly the same distributions (Gaussian, FWHM=3 mm), so that the final bracketed term in Eq. (13) would reduce to a value of 1. This assumption seemed reasonable based on our laboratory's experience with electron beams, and the final bracketed term should be relatively insensitive to small mismatches in the sizes of the two beams. Due to the design of the apparatus, it is very difficult to measure the electron-beam profile, and no definitive measurement of it was ever made. Since we acquire data at low electron energies, and we must keep our electron gun grids below 19 V to prevent ground-state excitation, the electron beam is not well collimated. There is also significant scattering of the electron beam by the atomic beam itself. This is why we have a segmented Faraday cup [12], with the first segment surrounding most of the collision region. Approximately 15–25% of the electron current was collected on the first segment of the Faraday cup at energies below 20 eV.

Due to the experimental design, it is physically impossible to translate a thin wire across the collision region in order to obtain an electron beam profile, as in the fast beam experiment described by Lagus *et al.* Instead, we assume a Gaussian distribution for our beam profile and use the electron current information provided by our segmented Faraday cup to determine the width of the beam at different positions along the Faraday cup. We obtain an estimate of the beam width at the end of each segment shown in Fig. 2 by calculating the FWHM of the Gaussian that would allow the measured percentage of the total current to pass through that segment. We then use a computer to fit a function for the beam width versus position in the Faraday cup to our measured data, and from this function obtain the beam width at the collision region. Using this technique, we calculate that the electron beam in the collision region has a FWHM of 5.5 mm.

D. Absolute calibration of the other $n\,^3L$ cross sections

Once the $2\,^3S \rightarrow 3\,^3P$ cross section is known, the cross sections for other triplet levels excited out of the $2\,^3S$ meta-

stable level can be obtained using a ratio technique. For a given upper level ($n\ ^3L$), we obtain both an excitation function out of the metastable level for energies up to about 18 eV, and an excitation function out of the ground state for energies up to 100 eV. For a given upper level ($n\ ^3L$), let us express the electron excitation signals as $(A\text{-}B)^{n\ ^3L}_{\rm meta}$ (10 eV) and $(A\text{-}B)^{n\ ^3L}_{\rm gs}$ (peak), which are the observed (A-B) counts for the $n\ ^3L \rightarrow m\ ^3K$ radiation due to metastable excitation (at 10 eV) and due to excitation from the ground state (at its peak), respectively, as follows:

$$(A\text{-}B)^{n\ ^3L}_{\rm meta}(10\ \text{eV}) = \xi_{n\ ^3L \rightarrow m\ ^3K} Q^{n\ ^3L}_{\rm meta}(10\ \text{eV}) \beta_{n\ ^3L \rightarrow m\ ^3K} \times \int \Omega(\vec{r}) n_{2\ ^3S}(\vec{r}) [J^{10\ \text{eV}}(\vec{r})/e] dV, \tag{16}$$

$$(A\text{-}B)^{n\ ^3L}_{\rm gs}(\text{peak}) = \xi_{n\ ^3L \rightarrow m\ ^3K} Q^{n\ ^3L}_{\rm gs}(\text{peak}) \beta_{n\ ^3L \rightarrow m\ ^3K} \times \int \Omega(\vec{r}) n_{\rm gs}(\vec{r}) [J^{\rm peak}(\vec{r})/e] dV. \tag{17}$$

We have already written similar equations for excitation into the $3\ ^3P$ level as Eqs. (3) and (4), for which we have obtained an absolute apparent cross section out of the metastable level (using LIF). We can now combine Eqs. (3), (4), (16), and (17) to obtain

$$Q^{n\ ^3L}_{\rm meta}(10\ \text{eV}) = \left[\frac{(A\text{-}B)^{n\ ^3L}_{\rm meta}(10\ \text{eV})/I^{10\ \text{eV}}}{(A\text{-}B)^{n\ ^3L}_{\rm gs}(\text{peak})/I^{\rm peak}} \right] \times \left[\frac{(A\text{-}B)^{3\ ^3P}_{\rm gs}(\text{peak})/I^{\rm peak}}{(A\text{-}B)^{3\ ^3P}_{\rm meta}(10\ \text{eV})/I^{10\ \text{eV}}} \right] \times \left[\frac{Q^{n\ ^3L}_{\rm gs}(\text{peak})}{Q^{3\ ^3P}_{\rm gs}(\text{peak})} \right] Q^{3\ ^3P}_{\rm meta}(10\ \text{eV}), \tag{18}$$

where the I's represent the total electron currents for the respective signals. We retain the I's next to their respective signals in the equation since the $n\ ^3L \rightarrow m\ ^3K$ and $3\ ^3P \rightarrow 2\ ^3S$ emissions may be measured under slightly different experimental conditions. This equation expresses the desired cross section in terms of eight experimentally measurable quantities, the four signals and their corresponding electron currents, and three known quantities, the two ground-state cross sections and the metastable cross section obtained through LIF. As long as the ground-state and metastable excitation functions for a given upper level are taken with the same optical and electronic systems, we can obtain an absolute cross section for any upper level. We note that all of the cross sections in the above formulas are *apparent* cross sections, where the apparent cross section is defined as the cross section for direct excitation into the specified level plus any cascade contribution [15]

$$Q^{\rm app}_j = Q^{\rm dir}_j + \sum_{i>j} Q^{\rm opt}(i \rightarrow j). \tag{19}$$

TABLE I. Sources of error for absolute calibration of $2\ ^3S \rightarrow 3\ ^3P$ cross section. Symbols shown are those used in Eq. (13) of the text.

Description		Contribution to Uncertainty
Metastable photon counting signal	$(A\text{-}B)^{3\ ^3P}_{\rm meta}$ (10 eV)	10%
Ground-state photon counting signal	$(A\text{-}B)^{3\ ^3P}_{\rm gs}$ (peak)	5%
Ground-state analog signal	$S_{\rm gs}$(peak)	5%
Electron current at 10 eV	$I^{10\ \text{eV}}$	2%
Electron current at ground-state peak	$I^{\rm peak}$	2%
Integrated LIF signal	$\int S_{\rm LIF}(\nu_L) d\nu_L$	20%
Laser Power	$w(\nu_0)$	15%
	Subtotal	28%
Optical profile	$\Omega(\vec{r})$	15%
Laser-beam profile	$w_0(\vec{r})$	15%
Electron-beam profile	$J_0^{10\ \text{eV}}(\vec{r})$	25%
Metastable-beam profile	$n_{2\ ^3S}(\vec{r})$	10%
	Profiles subtotal	34%
	Overall Uncertainty	45%

We also note that our absolute calibration only depends upon the ratios of the ground-state apparent cross sections used for the two given levels, not on their absolute magnitudes. The apparent cross sections for excitation out of the ground level are obtained from the results of St. John, Miller, and Lin [16], Jobe and St. John [17], and Moustafa Moussa, DeHeer, and Schutten [18]. All metastable cross sections obtained through this method are dependent on an accurate value for the $3\ ^3P$ cross section. Any time a revised value for the $3\ ^3P$, cross section is obtained, however, all the cross sections obtained through this ratio technique may be easily rescaled.

E. The $2\ ^3S \rightarrow 3\ ^3P$ excitation cross section

After all the beam profiles were obtained, we were able to calculate the integrals expressed in Eq. (13). In order to determine the sensitivity of our calculation to our beam profile measurements, we generously varied the beam parameters used in our analysis (electron beam FWHM 5.5 ± 2 mm, laser beam FWHM 0.75 ± 0.5 mm, optical profile FWHM 4.0 ± 1 mm). By far the largest contribution to the uncertainty of our absolute calibration is our lack of information about the size of the electron beam. With the above variations, we found the resulting uncertainty in the cross section to be $\pm 34\%$. This uncertainty estimate, along with the total uncertainty in the other measurements in Eq. (13) of $\pm 28\%$, gives an overall uncertainty of $\pm 45\%$. A summary of the various uncertainty contributions to our absolute calibration is given in Table I. We found a resulting $2\ ^3S \rightarrow 3\ ^3P$ electron excitation apparent cross section of $(2.2 \pm 1.0) \times 10^{-16}$ cm^2 at 10 eV. This result represents a significant change from the result of Rall *et al.*, which was $(3.0 \pm 1.0) \times 10^{-16}$ cm^2. Since we now have a more complete understanding of the beams in our experiment, this new result is more accurate. Subtracting

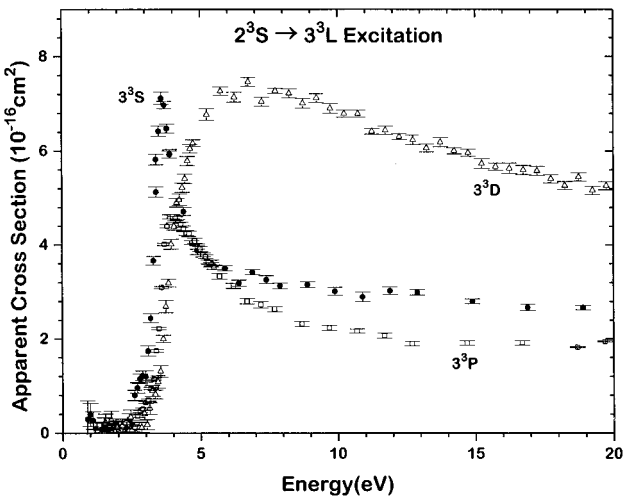

FIG. 4. Absolute apparent cross sections measured for excitation out of the $2\,^3S$ metastable level into the $n=3$ triplet levels. The error bars shown represent statistical error only, not the uncertainty due to the absolute calibration of the experiment.

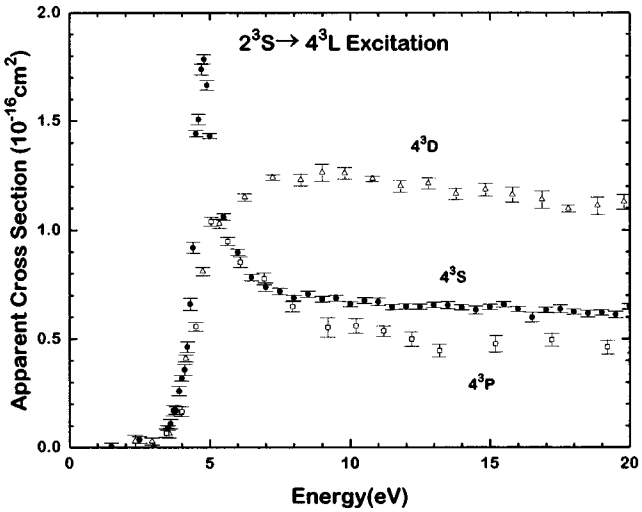

FIG. 5. Absolute apparent cross sections measured for excitation out of the $2\,^3S$ metastable level into the $n=4$ triplet levels. The error bars shown represent statistical error only, not the uncertainty due to the absolute calibration of the experiment.

cascade contributions, we obtain a $2\,^3S \rightarrow 3\,^3P$ direct electron excitation cross section of $(1.4\pm0.6)\times10^{-16}$ cm^2. Lagus *et al.*, with their completely independent absolute calibration of the fast beam experiment, obtained a cross section of $(1.6\pm0.6)\times10^{-16}$ cm^2, in excellent agreement with our experiment.

In comparison to the work of Rall *et al.*, our experiment involves a more detailed examination of the profiles of the electron beam, atomic beam, and laser beam. The effects of the overlaps of the various beams profiles on the excitation signals are analyzed in the present work. Our experiment also was carried out using a very low-power cw laser for the LIF calibration, whereas the experiment of Rall *et al.* used a high-power pulsed laser, for which checking for saturation effects can be difficult. One final point that should be made is that our experiment has a signal to noise about ten times higher than the experiment of Rall *et al.* This is primarily due to a higher metastable atom density in the target. The high signal to noise ratio in our experiment enables us to carry out diagnostic experiments that Rall *et al.* could not, and also enables us to obtain much improved measurements of the cross sections as functions of energy. We believe our present analysis to be more complete and accurate, and this gives results that are generally lower than those of Rall *et al.*

IV. RESULTS

A. The $n=3$, 4, and 5 levels

Figures 4–6 show excitation functions obtained using the techniques described in Sec. III and Table II contains all of our apparent cross-section results. All excitation functions are absolutely scaled by determining their cross sections at 10 eV. The $n=3$, 4, and 5 levels all show a pattern of sharply peaked excitation functions for the $2\,^3S \rightarrow n\,^3S$ and $2\,^3S \rightarrow n\,^3P$ excitations, and broad, fairly flat excitation functions for the $2\,^3S \rightarrow n\,^3D$. The peaks of the $2\,^3S \rightarrow n\,^3S$ excitation functions occur at lower energies and are distinctly sharper than the peaks of the $2\,^3S \rightarrow n\,^3P$ excitation functions. The $2\,^3S \rightarrow 5\,^3P$ excitation cross sections are not included in Fig. 6 and Table II because the signal-to-noise ratio of emissions that we have measured from the $5\,^3P$ level is too low to determine the cross sections with sufficient accuracy.

Figure 7 shows the onsets of the $3\,^3S$ and $3\,^3P$, and $3\,^3D$ excitation functions in greater detail. We make special note of the shoulders that occur in these onsets. For the $3\,^3S$ we observe a distinct bump that starts approximately 0.5 eV below the onset of the larger main peak of the excitation function. For the $3\,^3P$ and $3\,^3D$, we also observe shoulders in the onset of the excitation functions, although they are less distinct than in the case of the $3\,^3S$. We believe that these bumps may be due to the presence of $2\,^1S$ metastables in our atomic beam, which previous measurements have shown to be about 6–17% of the total number of metastables [10–12]. Because the $2\,^1S$ level is higher in energy than the $2\,^3S$, the

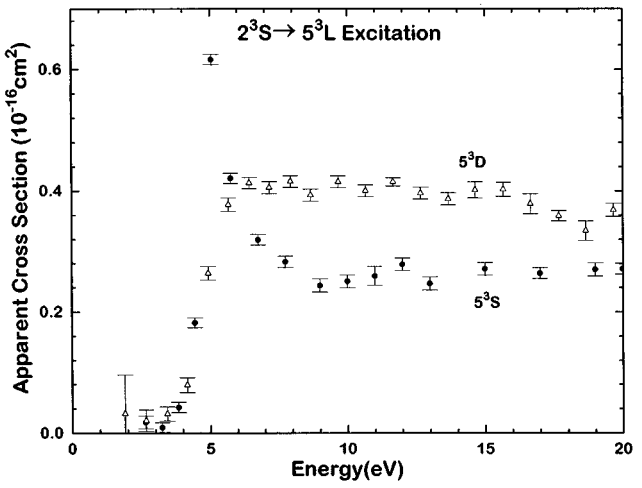

FIG. 6. Absolute apparent cross sections measured for excitation out of the $2\,^3S$ metastable level into the $n=5$ triplet levels. The error bars shown represent statistical error only, not the uncertainty due to the absolute calibration of the experiment.

TABLE II. Apparent cross sections for excitation of the $2\,^3S \rightarrow n\,^3L$ level of He measured by this experiment. All cross sections are in units of 10^{-16} cm^2. Absolute uncertainty of the cross sections is ±45%.

Incident Energy (eV)	$Q^{app}(2\,^3S \rightarrow n\,^3L)$								
	$2\,^3P$	$3\,^3S$	$3\,^3P$	$3\,^3D$	$4\,^3S$	$4\,^3P$	$4\,^3D$	$5\,^3S$	$5\,^3D$
2	80	0.00	0.00	0.00	0.00	0.00	0.00	0.00	0.00
3	113	1.20	0.65	0.20	0.00	0.00	0.00	0.00	0.00
4	117	5.70	4.56	4.40	0.33	0.15	0.41	0.12	0.07
5	116	3.88	3.90	6.40	1.42	1.06	0.92	0.62	0.26
6	110	3.50	3.20	7.30	0.87	0.86	1.12	0.36	0.39
7	109	3.30	2.81	7.25	0.75	0.77	1.20	0.30	0.42
8	108	3.15	2.45	7.20	0.70	0.63	1.26	0.28	0.42
9	107	3.05	2.25	7.10	0.69	0.57	1.27	0.27	0.41
10	106	3.01	2.23	6.79	0.66	0.56	1.26	0.25	0.40
12	95	3.01	2.00	6.35	0.64	0.47	1.20	0.27	0.41
14	84	2.91	1.90	5.70	0.64	0.46	1.18	0.27	0.40
16	80	2.75	1.84	5.40	0.63	0.44	1.14	0.27	0.39
18	78	2.71	1.75	5.20	0.62	0.44	1.11	0.27	0.37

onset of excitation into an $n\,^3L$ level out of the $2\,^1S$ level should occur 0.8 eV before the onset of excitation out of the $2\,^3S$ level. The energy spread of our electron beam is about 0.5 eV (FWHM). The $2\,^1S \rightarrow n\,^3L$ excitation functions should drop off rapidly with energy, since they are of the spin-changing type, in contrast to the $2\,^3S \rightarrow n\,^3L$ excitation functions. The relatively small percentage of $2\,^1S$ metastables, combined with the spin-changing nature of the $2\,^1S \rightarrow n\,^3L$ excitation, may account for the small size of the singlet bump relative to the triplet peak that follows. These small bumps thus show that we do observe a small amount of $2\,^1S \rightarrow n\,^3L$ excitation, but it should provide a negligible contribution to our $n\,^3L$ excitation functions, especially at energies significantly greater than onset because of the rapid

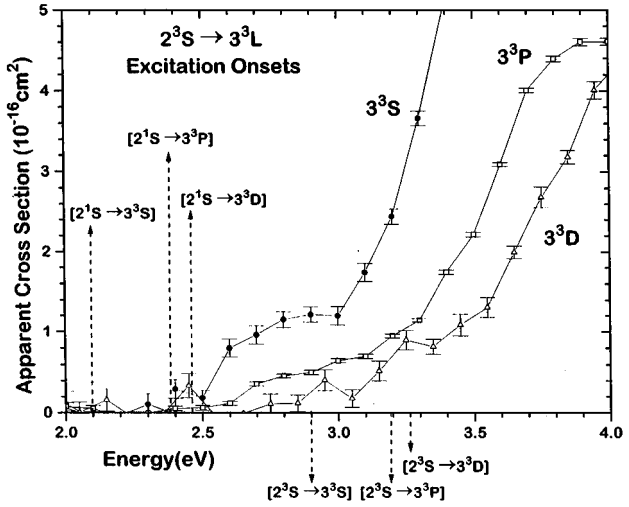

FIG. 7. Expanded view of the onset of excitation for the $n=3$ triplet levels. The error bars shown represent statistical error only. The threshold energies for excitation into the $n=3$ triplet levels out of the $2\,^3S$ level and out of the $2\,^1S$ levels are marked by the vertical lines.

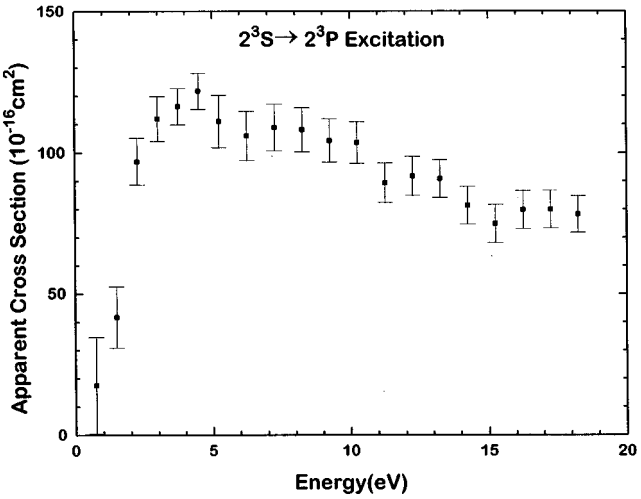

FIG. 8. Absolute apparent cross sections measured for excitation out of the $2\,^3S$ metastable level into the $2\,^3P$ level. The error bars shown represent statistical error only, not the uncertainty due to the absolute calibration of the experiment.

decrease in cross section with energy for singlet to triplet excitation.

B. The $2\,^3S \rightarrow 2\,^3P$ cross section

The cross section for excitation into the $2\,^3P$ level from the $2\,^3S$ level is of special interest. These two levels are only 1.1 eV apart, and the $2\,^3S \rightarrow 2\,^3P$ transition has a large oscillator strength, $f_{ik}(2\,^3S \rightarrow 2\,^3P)=0.5391$ versus $f_{ik}(2\,^3S \rightarrow 3\,^3P)=0.064\,46$, so one expects an extremely large electron excitation cross section. Unfortunately, the only emission out of the $2\,^3P$ level occurs at 1.08 μm in wavelength which is at the far edge of the photomultiplier sensitivity spectrum. We use an S-1 photocathode (Hammatsu R1767), specially selected for its sensitivity at this infrared wavelength. The quantum efficiency of the photocathode is generally less than 0.1% at this wavelength, greatly reducing the signal relative to what we could obtain for emission from other levels. To compound this problem, background radiation at this wavelength is large, due to the blackbody emission of the electron gun cathode, and due to light from the hollow cathode discharge. However, because of the extremely large size of the $2\,^3P$ cross section, we were able to observe an excitation function with signal to noise ratio comparable to that achieved with the $n=5$ levels. The observed excitation function is shown in Fig. 8.

The $2\,^3S \rightarrow 2\,^3P$ excitation function clearly does not show the sharp peak that we have observed for the $2\,^3S \rightarrow 3\,^3P$ and $2\,^3S \rightarrow 4\,^3P$ excitation functions. This shape difference may possibly be attributed to the energetic nearness of the $2\,^3P$ level to the $2\,^3S$ metastable level (1.1 eV) and to the ultrastrong collisional coupling between these two levels. In Na we find a similar trend in which the $3\,^2S \rightarrow 3\,^2P$ excitation function has a broader peak than the excitation functions for the higher members of the $3\,^2S \rightarrow n\,^2P$ family [14].

Our measured $2\,^3P$ peak apparent cross section is 117×10^{-16} cm^2, from which we obtain a peak direct cross section of 112×10^{-16} cm^2 (see Sec. IV C). This is a factor of 16 greater than the next largest peak direct cross section (the

$3\,^3D$) that we observed. Theoretical calculations also have predicted an enormous $2\,^3P$ direct cross section, as much as a factor of 20 larger than the $3\,^3D$ [1–7].

Muller-Fiedler *et al.* [19] have previously measured differential cross sections for He $2\,^3S \rightarrow 2\,^3P$ excitation. They used a cold-cathode discharge as the source of their metastable He, and obtained differential cross-section curves that matched well with the angular dependence of the differential cross section as calculated by Flannery and McCann [2]. However, Muller-Fiedler *et al.* obtained absolute values that were consistently a factor of about three larger than the calculations of Flannery and McCann. Due to the lack of small angle differential cross sections in the results of Muller-Fiedler *et al.*, we are unable to integrate their data to obtain a $2\,^3P$ integral cross section for comparison with our measurement.

C. Cascade contributions and direct excitation cross sections

With our more complete data set, we can now determine the cascade into the levels that we have observed. We do this by subtracting off from the apparent cross section the sum of all the optical emission cross sections that cascade into it, in accordance with Eq. (19). For example, the $3\,^3S$ apparent cross section contains a cascade contribution from the $3\,^3P \rightarrow 3\,^3S$ transition. Although we have not measured the $3\,^3P \rightarrow 3\,^3S$ emission cross section, we can obtain its value from our measured $3\,^3P \rightarrow 2\,^3S$ emission cross section, along with the Einstein A coefficients for the two transitions involved through the relation

$$Q^{\text{opt}}(3\,^3P \rightarrow 3\,^3S) = Q^{\text{opt}}(3\,^3P \rightarrow 2\,^3S) \times \frac{A(3\,^3P \rightarrow 3\,^3S)}{A(3\,^3P \rightarrow 2\,^3S)}. \tag{20}$$

We find that the $3\,^3P \rightarrow 3\,^3S$ cascade amounts to only 8.1% of the apparent cross section of the $3\,^3S$ level at 10 eV. Similarly, one finds that the $4\,^3P \rightarrow 3\,^3S$ cascade amounts to 1.7% of the apparent cross section of the $3\,^3S$ level at 10 eV. As mentioned earlier, we measured $5\,^3P \rightarrow 2\,^3S$ emission signal, but the signal-to-noise ratio in our experiment is too small to give reliable emission cross sections for this transition. Nevertheless, we used it to estimate the cascade from the $5\,^3P$ into the $3\,^3S$ (the $5\,^3P \rightarrow 3\,^3S$ emission cross section), and the $5\,^3P \rightarrow 3\,^3S$ cascade amounted to $<1\%$ of the $3\,^3S$ cross section. We have not measured excitation cross sections for levels with $n>5$, and therefore cannot experimentally determine their cascade from these levels. However, we can estimate their cross-section values by multiplying our measured $4\,^3P$ cross section by the ratio of the $n\,^3P$ to the $4\,^3P$ cross sections as calculated by the Born approximation (see explanation in Sec. V A). The cascade into the $3\,^3S$ from the $n\,^3P$ is then calculated using the this approximated $n\,^3P$ cross section and the appropriate branching ratio obtained from the transition probabilities [20,21]. We find the cascade into the $3\,^3S$ level from levels with $n>5$ to be $<1\%$ of the apparent cross section. We have performed a similar cascade analysis for the $4\,^3S$ level and $5\,^3S$ level.

The $2\,^3P$ level is most favorable for cascade analysis since we have directly measured the optical emission cross sections for the $n\,^3S \rightarrow 2\,^3P$ and $n\,^3D \rightarrow 2\,^3P$ cascades through $n=5$. We estimate the cross sections for the higher $n\,^3S$ and $n\,^3D$ levels by the procedure described in the last paragraph, and combine them with the appropriate branching ratios to obtain the $n\,^3S \rightarrow 2\,^3P$ and $n\,^3D \rightarrow 2\,^3P$ cascade cross sections for $n>5$. We find that 9% of the apparent cross section comes from cascade from the $n=3$ levels, 1% from cascade the $n=4$ levels, 0.4% from cascade from the $n=5$ levels, and 0.2% from cascade from the levels of $n=6$ through 10. This yields a cascade of about 11% of the apparent cross section. Using the same techniques, we find that for the $3\,^3P$ level 24% of the apparent cross section comes from cascade from the $n=4$ levels, 7% from cascade from the $n=5$ levels, and 7% from cascade from the levels of $n=6$ through 10. We have performed a similar analysis for the $4\,^3P$ level.

The $n\,^3P \rightarrow 3\,^3D$ emissions produce a negligible cascade correction (about 1%) to the $3\,^3D$ cross section because these emissions are relatively weak and because the $3\,^3D$ cross section is large. We have, however, no knowledge of the $n\,^3F \rightarrow 3\,^3D$ cascade because excitation cross sections out of the $2\,^3S$ into the F states have not been measured. In the absence of experimental data we neglect the cascade from the F levels. In view of the very large $3\,^3D$ cross section, this approximation is likely to be valid, but experimental measurements are needed for a definitive answer. For the $4\,^3D$ and $5\,^3D$ level similar analyses show the cascade corrections due to emission from the $n\,^3P$ levels are much less than the experimental uncertainty of the apparent cross sections. The cascade from the $n\,^3F$ levels are again neglected. The direct excitation cross sections from 2 to 18 eV for the various levels studied are shown in Table III.

TABLE III. Direct cross sections for excitation of the $2\,^3S \rightarrow n\,^3L$ level of He estimated from apparent cross-section measurements of this experiment. All cross sections are in units of 10^{-16} cm^2. Absolute uncertainty of the cross sections is $\pm 45\%$.

Incident Energy (eV)	$Q^{\text{dir}}(2\,^3S \rightarrow n\,^3L)$								
	$2\,^3P$	$3\,^3S$	$3\,^3P$	$3\,^3D$	$4\,^3S$	$4\,^3P$	$4\,^3D$	$5\,^3S$	$5\,^3D$
2	80.5	0.00	0.00	0.00	0.00	0.00	0.00	0.00	0.00
3	112.0	1.13	0.65	0.20	0.00	0.00	0.00	0.00	0.00
4	106.3	5.19	4.29	4.39	0.33	0.12	0.41	0.12	0.07
5	103.6	3.30	2.68	6.31	1.38	0.79	0.89	0.61	0.25
6	96.5	3.02	2.23	7.22	0.84	0.65	1.09	0.35	0.37
7	95.7	2.88	1.89	7.18	0.71	0.58	1.17	0.29	0.40
8	95.0	2.79	1.54	7.14	0.67	0.44	1.24	0.27	0.41
9	94.2	2.72	1.36	7.05	0.67	0.39	1.25	0.27	0.40
10	93.7	2.68	1.37	6.74	0.64	0.38	1.24	0.25	0.39
12	83.5	2.71	1.14	6.31	0.62	0.29	1.18	0.27	0.40
14	73.6	2.63	1.05	5.66	0.62	0.28	1.16	0.27	0.39
16	70.2	2.48	1.01	5.36	0.61	0.26	1.12	0.27	0.38
18	67.6	2.45	0.93	5.16	0.60	0.26	1.09	0.27	0.36

D. Comparison with previous experiments

Lagus *et al.* [13] recently reported measurements of excitation cross sections out of the He($2\,^3S$) metastable level into the $3\,^3S$, $3\,^3D$, and $4\,^3D$ levels up to 600 eV. They produced their metastable target by charge exchange of Cs atoms with a He^+ beam at 1.6 keV. The resulting fast metastable beam

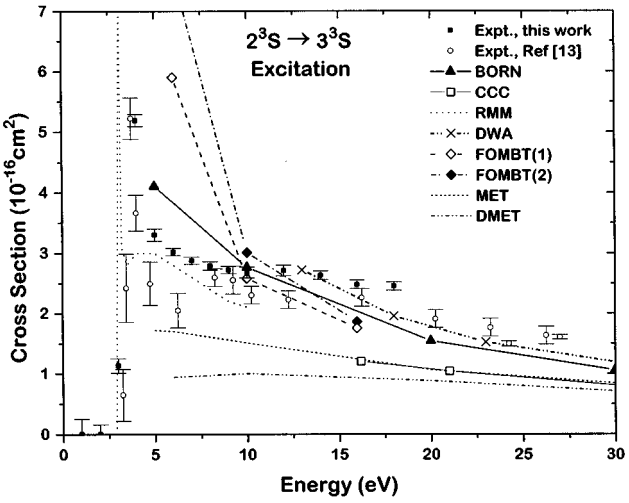

FIG. 9. Comparison of direct excitation cross sections of this experiment and those of Lagus *et al.* [13] with various theoretical calculations for $2\,^3S \rightarrow 3\,^3S$ excitation. The error bars shown represent statistical error only.

has only a small fraction of ground-state He atoms, so that they were able to study excitation out of the metastable level at energies above the onset for ground-state excitation. They obtained absolute cross sections by measuring the metastable beam density, electron-beam density, and the fluorescence resulting from the electron-impact excitation out of the $2\,^3S$ metastable level and out of the ground level. Thus their method of absolute calibration is entirely different from the LIF technique described in Sec. III. At 10 eV their cross sections, in units of 10^{-16} cm^2, for the $3\,^3S$, $3\,^3D$, and $4\,^3D$ levels are 2.5, 1.6, 6.3, and 1.1, respectively, in good agreement with the corresponding results of 2.7, 1.4, 6.7, and 1.2 from the present work. We also compare the cross sections from the two experiments at other energies in Figs. 9–11 and the agreement is very good.

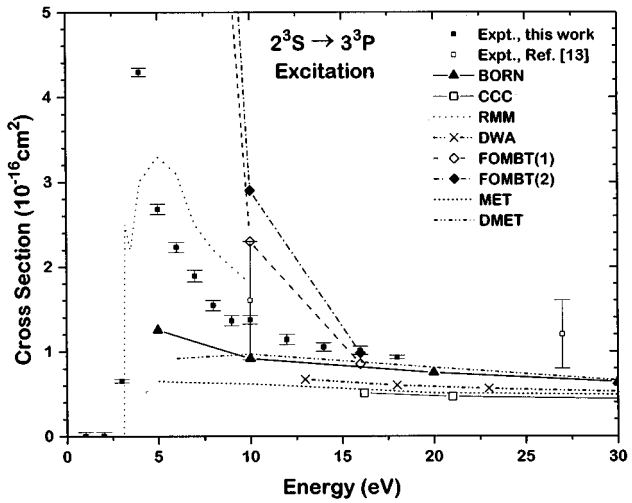

FIG. 10. Comparison of direct excitation cross sections of this experiment and the measurements of Lagus *et al.* [13] with various theoretical calculations for $2\,^3S \rightarrow 3\,^3P$ excitation. The experimental results are shown with statistical error bars only.

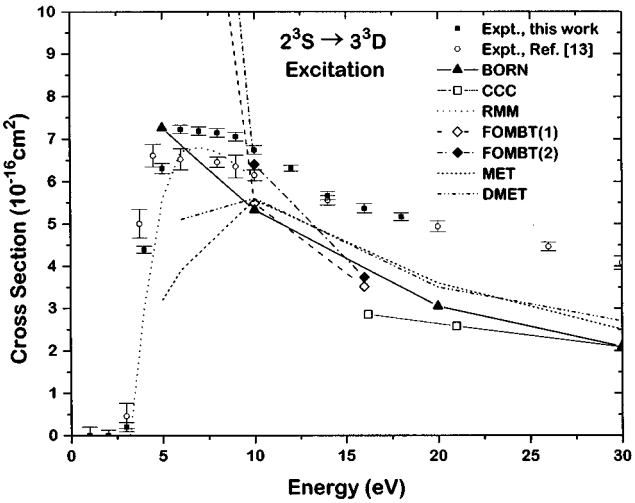

FIG. 11. Comparison of direct excitation cross sections of this experiment and those of Lagus *et al.* [13] with various theoretical calculations for $2\,^3S \rightarrow 3\,^3D$ excitation. The error bars shown represent statistical error only.

The cross sections of Lagus *et al.* differ drastically from those reported by Gostev *et al.* and by Mityureva and Penkin [8,9]. In Ref. [13] Lagus *et al.* compared their data with those of Refs. [8] and [9]. Since our results are very close to those of Lagus *et al.*, we have no further comments to add.

E. Comparison with theoretical calculations

Lagus *et al.* have presented a detailed comparison of their $2\,^3S \rightarrow 3\,^3S$ and $2\,^3S \rightarrow 3\,^3D$ excitation cross sections with theoretical calculations based on numerous different methods: the multichannel eikonal theory (MET) [2], the *R*-matrix method (RMM) [6], the distorted-wave approximation (DWA) [5], the updated multichannel eikonal theory (DMET) [3], two versions of the first-order many-body theory (FOMBT) [7], and the convergent close-coupling method (CCC) [4]. In Figs. 9–12 we display the theoretical values calculated by the various methods, along with our own experimental results (and also of Ref. [13] where available), in the 0–30 eV energy range for the $2\,^3S \rightarrow 3\,^3S$, $2\,^3S \rightarrow 3\,^3P$, $2\,^3S \rightarrow 3\,^3D$, and $2\,^3S \rightarrow 2\,^3P$ excitation functions. Also included for comparison are the Born-approximation cross sections [1]. The curves for the theoretical values in those figures are obtained by joining the cross-section values given in the original papers. A critical analysis of the results of the different sets of calculation is beyond the scope of this paper. On the whole, the RMM exhibits the most consistent agreement with our experimental data. The large spread of the theoretical cross sections based on different methods is a reflection of the difficulty of an accurate theoretical treatment of electron-impact excitation out of excited states. It is gratifying to see the increased level of theoretical efforts in this subject in recent years.

V. DISCUSSION

A. Magnitude of the excitation cross sections

The He $2\,^3S \rightarrow 2\,^3P$ excitation cross section that we obtain (11.2×10^{-15} cm^2 at the peak of the excitation function) is an exceptionally large cross section. A similar excitation

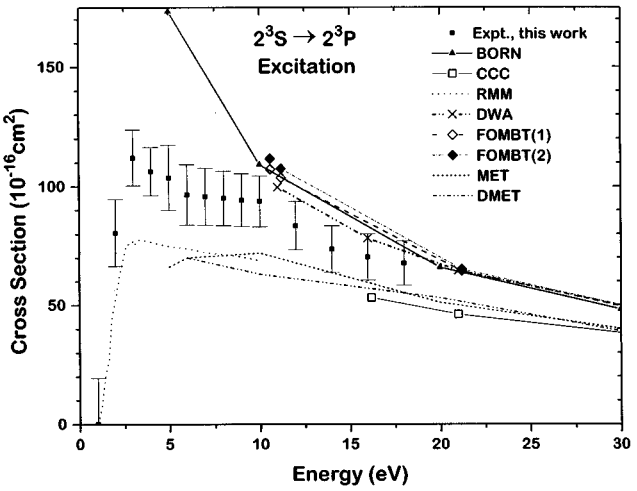

FIG. 12. Comparison of the direct excitation cross sections of this experiment with various theoretical calculations for $2\,^3S \rightarrow 2\,^3P$ excitation. The experimental results are shown with statistical error bars only.

process is the excitation of the first resonant level in the alkali-metal atoms for which the peak cross sections are 4.1×10^{-15} cm^2 for Li($2\,^2S \rightarrow 2\,^2P$), 3.6×10^{-15} cm^2 for Na($3\,^2S \rightarrow 3\,^2P$), and 4.7×10^{-15} cm^2 for K($4\,^2S \rightarrow 4\,^2P$) [23,14,22]. While these three alkali-metal cross sections are rather close, they are about three times smaller then the He cross section. In fact, the case of He($2\,^3S \rightarrow 2\,^3P$) represents the largest electron-atom excitation cross section that we are aware of.

For excitation out of the $2\,^3S$ level into the higher n levels an obvious feature is that the $n\,^3P$ level has the smallest cross section among the triplet levels of the same n. This is in contrast with the trend observed for excitation out of the ground level of He, for which electron excitation into levels corresponding to dipole-allowed optical transitions have much larger cross sections than excitations into dipole-forbidden levels of the same n. While theoretical calculations based on several different methods predict a smaller cross section for the $2\,^3S \rightarrow 3\,^3P$ than the $2\,^3S \rightarrow 3\,^3S$ and $2\,^3S \rightarrow 3\,^3D$ excitations, such a reversal in the relative magnitudes appears surprising at first sight. To better understand it, let us draw an analogy between electron excitation and optical excitation and associate the $2\,^3S \rightarrow n\,^3P$ and $2\,^3S \rightarrow n\,^3D$ electron excitations with the optical dipole and quadrupole absorptions, respectively. This analogy is quantitative only for forward scattering, but we apply it here to the integrated cross sections for the purpose of illustration. The dipole matrix elements for the $2\,^3S \rightarrow n\,^3P$, $m=0$ series satisfy the sum rule

$$\sum_n |\langle 2\,^3S|z|n\,^3P,\ m=0\rangle|^2 = \langle 2\,^3S|z^2|2\,^3S\rangle. \qquad (21)$$

The $2\,^3S$ and $2\,^3P$ levels are close together and their radial wave functions overlap strongly, so that the matrix element between them is exceptionally large. The constraint of the sum rule tends to reduce the other matrix elements in the series. Carrying this analogy to electron-impact excitations, we see that the $2\,^3S \rightarrow 3\,^3P$ excitation cross section is reduced because of the unusually large $2\,^3S \rightarrow 2\,^3P$ cross section. For the $2\,^3S \rightarrow n\,^3D$ excitation one has the quadrupole sum rule,

$$\sum_n |\langle 2\,^3S|2z^2-x^2-y^2|n\,^3D,m=0\rangle|^2 = \langle 2\,^3S|(2z^2-x^2-y^2)^2|2\,^3S\rangle, \qquad (22)$$

but there are no corresponding extraordinary large cross sections analogous to the $2\,^3S \rightarrow 2\,^3P$ excitation to reduce the $2\,^3S \rightarrow 3\,^3D$ cross section.

For excitation out of the ground state, one also has the sum rule of the form

$$\sum_n |\langle 1\,^1S|z|n\,^1P,\ m=0\rangle|^2 = \langle 1\,^1S|z^2|1\,^1S\rangle. \qquad (23)$$

However, the $\langle 1\,^1S|z|2\,^1P\rangle$ matrix element is not exceptionally large, and it does not cause a severe reduction of the matrix elements of the higher members the way the $\langle 2\,^3S|z|2\,^3P\rangle$ element does. This is reflected by the relative cross sections. The ratio of the $1\,^1S \rightarrow 2\,^1P$ to the $1\,^1S \rightarrow 3\,^1P$ excitation cross section (peak values) is about 3:1, whereas in the case of electron-impact excitation out of the $2\,^3S$ level, the ratio of the $2\,^3S \rightarrow 2\,^3P$ cross section to the $2\,^3S \rightarrow 3\,^3P$ cross section at 10 eV is 69:1. An explanation of a similar nature offered by Flannery and McCann [2] is that the reduction of the $2\,^3S \rightarrow 3\,^3P$ excitation cross section results from the overlap between the $2s$ and $2p$ radial wave functions and the orthogonality between the $2p$ and $3p$ orbitals.

It is also possible to apply the same considerations to Na atoms. The $\langle 3s|z|3p\rangle$ matrix element is known to be enormous. The cross sections for excitation from the $3\,^2S$ into the higher $n\,^2P$ levels are small compared to the cross section for excitation into the $3\,^2P$ level. For instance, at 10 eV the cross sections for excitation from the $3\,^2S$ level of Na into the $3\,^2P$, $4\,^2P$, $5\,^2P$, and $6\,^2P$ are 35.6×10^{-16} cm^2, 0.585×10^{-16} cm^2, 0.143×10^{-16} cm^2, and 0.0411×10^{-16} cm^2, respectively [14]. Here we see a drastic drop from the lowest member to the next higher one (a factor of 60), but a much more gentle variation above the $4\,^2P$. For the diffuse series in Na, the excitation cross sections for the $3\,^2D$, $4\,^2D$, $5\,^2D$, and $6\,^2D$ levels at 10 eV are 3.67×10^{-16} cm^2, 0.842×10^{-16} cm^2, 0.346×10^{-16} cm^2, and 0.168×10^{-16} cm^2, respectively [14]. The reduction factor is 4.4 from the $3\,^2D$ to the $4\,^2D$ and 2.4 from the $4\,^2D$ to $5\,^2D$, in contrast to the much more drastic reduction in the $n\,^2P$ series. Here the $n\,^2P$ cross sections are seen to be smaller than the corresponding $n\,^2D$ for $n=4$, 5, and 6, similar to excitation out of the He($2\,^3S$) level.

Table III also shows that the $2\,^3S \rightarrow 4\,^3P$ excitation cross sections of He are also smaller than the corresponding $2\,^3S \rightarrow n\,^3S$ and $2\,^3S \rightarrow n\,^3D$ cross sections. Preliminary measurements (not shown in Tables II or III) suggest that the $5\,^3P$ cross section is also smaller than the $5\,^3S$ and $5\,^3D$ cross section. It is also interesting to note the same trend in Na, i.e., both the $3\,^2S \rightarrow n\,^2S$ and $3\,^2S \rightarrow n\,^2D$ cross sections are larger than the $3\,^2S \rightarrow n\,^2P$ cross sections.

While Figs. 9–12 show only moderate agreement of the Born cross sections with the experimental values, it is, nevertheless, instructive to use the Born approximation to analyze the trend of variation of the excitation cross sections

TABLE IV. Direct cross-section ratios obtained from experiment and from the Born approximation.

	Experiment (10 eV)	Born (10 eV)	Born (40 eV)
$Q(2\,^3S\rightarrow 3\,^3S)/Q(2\,^3S\rightarrow 4\,^3S)$	4.2	4.9	4.8
$Q(2\,^3S\rightarrow 4\,^3S)/Q(2\,^3S\rightarrow 5\,^3S)$	2.6	2.6	2.6
$Q(2\,^3S\rightarrow 2\,^3P)/Q(2\,^3S\rightarrow 3\,^3P)$	69	118	67
$Q(2\,^3S\rightarrow 3\,^3P)/Q(2\,^3S\rightarrow 4\,^3P)$	3.6	3.7	3.2
$Q(2\,^3S\rightarrow 3\,^3D)/Q(2\,^3S\rightarrow 4\,^3D)$	5.4	4.1	4.2
$Q(2\,^3S\rightarrow 4\,^3D)/Q(2\,^3S\rightarrow 5\,^3D)$	3.2	2.5	2.5

with n for each L family and compare this with our measurements. In Table IV we list the values of the cross-section ratios $Q(2\,^3S\rightarrow n\,^3L)/Q(2\,^3S\rightarrow[n+1]\,^3L)$ for the S, P, and D series obtained from our measurements at 10 eV and from Born calculations at 10 and 40 eV. The Born cross-section ratios are nearly the same at the two electron energies shown for the $2\,^3S\rightarrow n\,^3L$ excitations except for the ratio involving $Q(2\,^3S\rightarrow 2\,^3P)$. We see a reasonable agreement in the cross-section ratios between the Born calculations and our experimental data. The results shown in Table IV suggest that in the absence of experimental measurement an estimate of the $2\,^3S\rightarrow n\,^3L$ excitation cross section for a high-n level can be obtained by using the Born approximation to calculate the $Q(2\,^3S\rightarrow n\,^3L)/Q(2\,^3S\rightarrow 4\,^3L)$ and taking the product of this ratio times the experimental value of $Q(2\,^3S\rightarrow 4\,^3L)$.

B. Shape of the excitation functions

One can also compare the shapes of the He$(2\,^3S\rightarrow n\,^3L)$ excitation functions to the shapes of the excitation functions out of the ground states of the Na [14] and Li [23,24] into the corresponding excited states. Figures 13–15 show some of these comparisons. In Fig. 13 we plot the normalized results (normalized at 10 eV) of the He$(2\,^3S\rightarrow 2\,^3P)$ excitation function along with those of the Li$(2\,^2S\rightarrow 2\,^2P)$ and Na$(3\,^2S\rightarrow 3\,^2P)$ excitation functions. These three curves represent excitation into the first P level above the initial level. One can see that all three curves have relatively flat maxima, with the He$(2\,^3S\rightarrow 2\,^3P)$ declining slightly faster with increasing energy than the two alkalis. Figure 14 shows excitation functions into the first S level above the initial level—He$(2\,^3S\rightarrow 3\,^3S)$, Li$(2\,^2S\rightarrow 3\,^2S)$, and Na$(3\,^2S\rightarrow 4\,^2S)$. These excitation functions show remarkable similarity in shape, with all three having a narrow peak just after onset. Likewise, one can compare excitation functions into the first D levels—He$(2\,^3S\rightarrow 3\,^3D)$, Li$(2\,^2S\rightarrow 3\,^2D)$, and Na$(3\,^2S\rightarrow 3\,^2D)$. Figure 15 shows that the curves for the He$(2\,^3S\rightarrow 3\,^3D)$ and Li$(2\,^2S\rightarrow 3\,^2D)$ are very alike, whereas the Na$(3\,^2S\rightarrow 3^2D)$ excitation function shows appreciable deviation below 7 eV. For further comparison we also plot in Fig. 15 the shape of the Na$(3\,^2S\rightarrow 4\,^2D)$ excitation function which is seen to be remarkably close to the He and Li curves.

In Fig. 16 we show the shape of the excitation functions, calculated by the Born approximation [25], for excitation out of the $2\,^3S$ into the $3\,^3S$, $3\,^3P$, and $3\,^3D$. The $3\,^3P$ excitation function has the sharpest peak near the onset but declines more slowly at higher energies, whereas the $3\,^3S$ and $3\,^3D$ excitation functions are rather similar. This trend is different from our experimental observation of the $3\,^3D$ excitation function having the broadest peak and the $3\,^3S$ the narrowest. Although the experimental data shown in Fig. 4 are the apparent excitation functions, the same trend holds for the direct excitation functions. We can also examine the variations of the excitation functions within a series of $2\,^3S\rightarrow n\,^3L$ excitations ($n\geqslant 3$) for a given L. The shapes of the excitation functions calculated by the Born approximation for different n within an L series are very similar, and the same is true of the measured excitation functions (Figs. 4–6) even though the theoretical and experimental shapes do not agree well with each other. Because of this constancy in the shape of the excitation functions for a given L, the ratio of

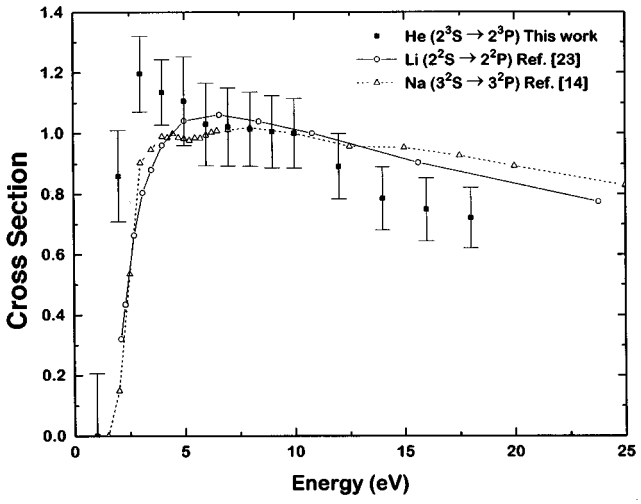

FIG. 13. Comparison of the experimentally observed shapes of direct cross section vs energy for excitation into the first P level above the initial level for He$(2\,^3S)$, Li$(2\,^2S)$, and Na$(3\,^2S)$. All excitation functions are normalized to unity at 10 eV.

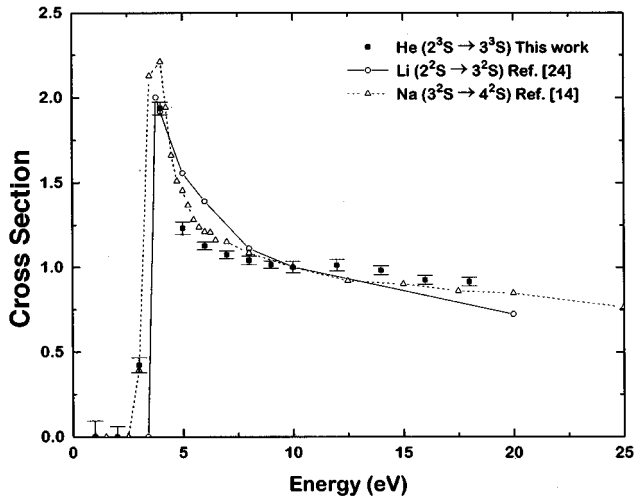

FIG. 14. Comparison of the experimentally observed shapes of cross section vs energy for excitation into the first S level above the initial level for He$(2\,^3S)$, Li$(2\,^2S)$, and Na$(3\,^2S)$. The He and Na data are direct excitation cross sections but the Li curve includes cascade contributions. All excitation functions are normalized to unity at 10 eV.

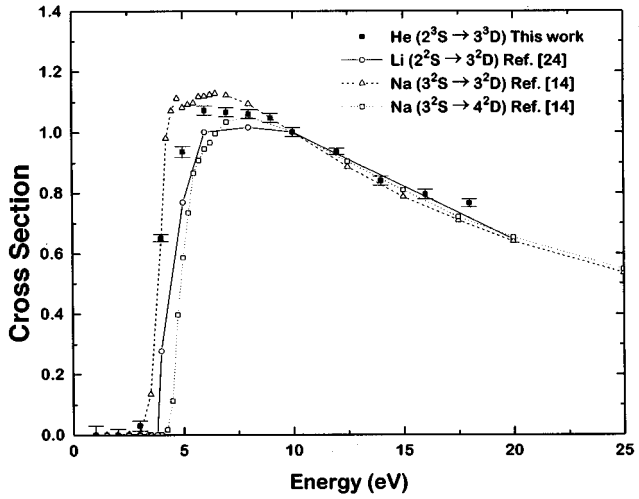

FIG. 15. Comparison of the experimentally observed shapes of direct cross section vs energy for excitation into the first D level above the initial level for He($2\,^3S$), Li($2\,^2S$), and Na($3\,^2S$). The He and Na data are direct excitation cross sections but the Li curve includes cascade contributions. For additional comparison the excitation function for Na($3\,^2S \rightarrow 4\,^2D$) is also shown. All excitation functions are normalized to unity at 10 eV.

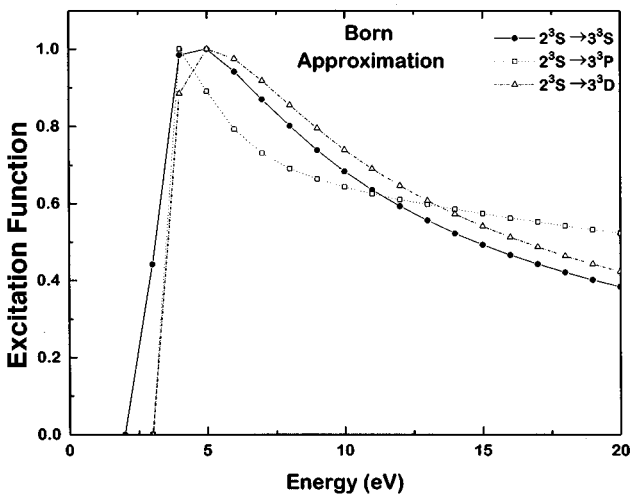

FIG. 16. Comparison of shapes of excitation functions for He($2\,^3S \rightarrow 3\,^3L$) excitation obtained by Born approximation calculation at low energies. The peak cross section for each curve is normalized to unity.

$Q(2\,^3S \rightarrow n\,^3L)/Q(2\,^3S \rightarrow n'\,^3L)$, with n, $n' > 2$, is nearly independent of the electron energy, and provides a means of extrapolating the measured cross sections to higher n, as suggested in Sec. V A. On the other hand, the ratio of cross sections across two L families, $Q(2\,^3S \rightarrow n\,^3L)/Q(2\,^3S \rightarrow n'\,^3L')$, is generally energy dependent, and is not as useful a parameter for extrapolation.

C. Overview of the He($2\,^3S$) and alkali cross sections

In this section we analyze the cross sections for excitation out of the metastable He($2\,^3S$) level in relation to the excitation cross sections out of the ground levels of the alkali-metal atoms. Since this is an initial step toward a more comprehensive study, we limit ourselves to excitation into the first P level, i.e., He($2\,^3S \rightarrow 2\,^3P$), K($4\,^2S \rightarrow 4\,^2P$), etc. As a guide to our approach we start with Born theory. For excitation corresponding to dipole-allowed transitions, the Born theory may be simplified by the Bethe approximation. For the case of He($2\,^3S \rightarrow 2\,^3P$) excitation, calculations [1] show that the Born-Bethe procedure reproduces the full Born calculation down to an energy of about 3 eV. For electron excitation out of level i of degeneracy g_i into level j of degeneracy g_j the Bethe-Born cross section is [26]

$$Q^{BB}(i \rightarrow j) = \frac{4\pi a_0^2}{E/R}\left[\frac{S_{ij}}{3g_i}\ln\frac{4c_{ij}E}{R} + \frac{\gamma_{ij}}{E/R}\right], \qquad (24)$$

where a_0 is the Bohr radius, R is the Rydberg energy (13.6 eV), and S_{ij} is the line strength of an N-electron system defined by

$$S_{ij} = \sum_{m_i m_j} \left|\left\langle m_i \left| -e\sum_{s=1}^{N} \vec{r}_s \right| m_j \right\rangle\right|^2, \qquad (25)$$

with m_i and m_j being the sublevel indices. If we define the excitation energy E_{ji} as $E_j - E_i$, the oscillator strength can be written as

$$f_{ij} = (E_{ji}/R)(S_{ij}/3g_i). \qquad (26)$$

The parameters c_{ij} and γ_{ij} can be determined, in principle, from full knowledge of the inelastic form factor $\langle \Psi_i | \Sigma_s \exp(i\vec{K}\cdot\vec{r}_s) | \Psi_j \rangle$ as a function of the momentum change $\hbar K$ that the electron suffered in the collision. The logarithmic term in Eq. (24) originates [27] from $\ln(K_{\max}^2/K_{\min}^2)$ where the minimum momentum change is given by $K_{\max}^2 a_0^2 \approx (E_{ji}/R)^2/(2E/R)$. The radial integral $\langle P_i(r) | j_1(Kr) | P_j(r) \rangle$ of the form factor is mainly determined by the range r of the more compact of the two radial atomic functions in that integral, i.e., $P_i(r)$, via $\overline{Kr} \lesssim 1$ due to the canceling effect of the oscillations of the Bessel function $j_1(\kappa r)$ for $\overline{Kr} > 1$. The maximum practical K is therefore given by $(Ka_0)^2 \approx 1/n_1^2 = I_i/R$, where n_i and I_i are the principal quantum number and ionization potential of the initial state, respectively. Hence,

$$c_{ij} = \overline{(Ka_0)}^2/(E_{ji}/R)^2 \approx I_i R/E_{ji}^2 \qquad (27)$$

is a satisfactory approximation for our discussion of the relations among the He($2\,^3S$) and alkali-metal cross sections.

One advantage of the Born-Bethe theory is that it connects the excitation cross section to atomic parameters in a simple form. Since our measured He($2\,^3S$) excitation cross sections are limited to $E \leqslant 18$ eV, we do not compare them quantitatively with the Born-Bethe calculations. Instead we attempt to find correlations between the measured cross sections of the He, Li, Na, K series with the relevant atomic parameters even though the mathematical functional dependence of Eq. (24) is not satisfied. In Table V we list the line strength, oscillator strength, excitation energy, ionization energy, and the polarizability of the initial state, along with the peak cross sections for the $n_i S \rightarrow n_i P$ excitation, where n_i is the principal quantum number of the initial state [20,28–31]. Motivated by Eq. (27) we also list the values of $I_i R/E_{ji}^2$.

Let us first compare only the three alkali-metal atoms,

TABLE V. Peak excitation cross sections Q (in units of 10^{-15} cm^2) and atomic properties (in atomic units unless otherwise noted).

	He($2\,^3S\rightarrow 2\,^3P$)	Li($2\,^2S\rightarrow 2\,^2P$)	Na($3\,^2S\rightarrow 3\,^2P$)	K($4\,^2S\rightarrow 4\,^2P$)
$Q(i\rightarrow j)$	11.2	4.1	3.6	4.7
S_{ij}/g_i	19.2	16.7	19.1	25.8
f_{ij}	0.539	0.753	0.982	1.02
I_i (eV)	4.77	11.2	5.14	4.34
E_{ji} (eV)	1.15	1.85	2.10	1.61
I_iR/E_{ji}^2	49.4	21.3	15.8	22.8
α_i	316	165	166	303

leaving out He for the moment. The cross sections are not entirely on the order of the line strength as Na has the smallest cross section, but its line strength is larger than that of Li. Sodium has the largest excitation energy which may tend to decrease the cross section. This difference is accentuated if we look at the I_iR/E_{ji}^2 parameter which has a substantially smaller value for Na than for Li. Here it appears that the line strength has a primary influence on the cross section, but a small I_iR/E_{ji}^2 may compensate for a larger S_{ij} to yield a smaller cross section. Included in Table V is the polarizability which does not appear in the Born-Bethe formula. For slow collisions the importance of the polarization interaction is well known. Even at higher impact energies the polarizability is still a relevant parameter for the alkali-metal atoms. Consider, for instance, the case of Na. The dipole matrix element $|\langle 3S|\vec{r}|3P\rangle|^2$ is so much larger than the ones connecting the $3S$ state with the higher P states that the second-order perturbation formula for the polarizability can be approximated by just the leading term, which is proportional to $S_{3S,3P}/E_{3S,3P}$. Indeed Table V shows that the cross sections almost follow the same trends as the polarizability of the initial state. This is a manifestation of the importance of the influence of the line strength on the cross section as modified by E_{ij}.

We now include He in our consideration to see whether the relations between the cross section and the atomic parameters conform to the pattern discussed in the preceding paragraph. The most obvious feature is that the He cross section is much larger than the alkali-metal-atom cross sections, whereas the atomic parameters, except I_iR/E_{ji}^2, exhibit much less variation. The qualitative pattern is still consistent with the cross sections being influenced by the combined effects of S_{ij}/g_i and I_iR/E_{ji}^2, but the former no longer dominates the cross section. For instance, He has three times the cross section of Na, yet their values of S_{ij}/g_i are nearly the same. Likewise K has a significantly larger S_{ij}/g_i (34%) but a much smaller cross section (less than half) than He. Of course the effects of line strength and excitation energy are not strictly separable. Nevertheless, our goal is to seek a simple picture to understand the gross features of the cross sections in terms of atomic parameters. In this regard we find He($2\,^3S$) very different from the alkali-metal atoms in spite of similarities in their atomic structure. While the numbers in Table V suggest that the small excitation energy in He may be related to its much larger cross section, further efforts must be made to arrive at a picture that would provide a unified understanding of the excitation behaviors of He($2\,^3S$) and the alkali-metal atoms.

As a note of interest, we see from Table V that a large line strength, rather than a large oscillator strength, results in a large excitation cross section. This is understandable since it is S_{ij} not f_{ij}, that appears as a multiplicative factor in the first term of Eq. (24). The smaller f_{ij} in He results from the small excitation energy.

VI. CONCLUSIONS

We have obtained absolute apparent cross sections for excitation out of the $2\,^3S$ level of He into nine higher triplet levels. We have performed a new absolute calibration of these cross sections, and our results agree well with the cross sections reported by Lagus *et al.* from their fast beam experiments that used an entirely different method for absolute calibration. From these data we have also been able to determine the direct cross sections for excitation into these levels. Of special note, we have measured the extremely large $2\,^3S\rightarrow 2^3P$ cross section for the first time. For excitation out of the $2\,^3S$ level the cross sections for the optically allowed levels ($n\,^3P$) are smaller than the cross sections for the $n\,^3D$ and $n\,^3S$ levels. This is in contrast to the case of excitation out of the ground levels where the $n\,^1P$ levels have much larger cross sections than the $n\,^1D$ and $n\,^1S$. This reversal behavior is explained on the ground that the extraordinarily large cross sections for the $2\,^3S\rightarrow 2\,^3P$ excitation causes a reduction of the cross section for the higher members of the $n\,^3P$ series. For $n=3$, 4, and 5, our excitation functions show a pattern of sharply peaked excitation functions for the $n\,^3S$ and $n\,^3P$ levels, and broad excitation functions for the $n\,^3D$ levels. The $2\,^3P$ excitation, however, has a distinctly flatter excitation function than the higher $n\,^3P$ levels. We have made comparisons with the electron excitation of the ground levels of the alkali-metal atoms in order to provide a more unified view toward understanding the excitation behaviors of both He($2\,^3S$) and the alkali-metal atoms.

ACKNOWLEDGMENTS

This work was supported in part by the National Science Foundation. The authors wish to thank John B. Boffard for his considerable assistance. We are grateful to Dr. S. Chung for providing us with the Born approximation cross sections used in this paper. We would also like to thank R. B. Lockwood and C. M. Martin for their contributions in bringing this paper to completion.

[1] D. Ton-That, S. T. Manson, and M. R. Flannery, J. Phys. B **10**, 621 (1977); M. R. Flannery, W. F. Morrison, and B. L. Richmond, J. Appl. Phys. **46**, 1186 (1975).
[2] M. R. Flannery and K. J. McCann, Phys. Rev. A **12**, 846 (1975).
[3] E. J. Mansky and M. R. Flannery, J. Phys. B **25**, 1591 (1992).
[4] I. Bray and D. V. Fursa, J. Phys. B **28**, L197 (1995).
[5] K. C. Mathur, R. P. McEachran, L. A. Parcell, and A. D. Stauffer, J. Phys. B **20**, 1599 (1987).
[6] K. A. Berrington, P. G. Burke, L. C. G. Freitas, and A. E. Kingston, J. Phys. B **18**, 4135 (1985).
[7] D. C. Cartwright and G. Csanak, Phys. Rev. A **51**, 454 (1995).
[8] V. A. Gostev, D. V. Elakhovskii, Y. V. Zaitsev, L. A. Luizova, and A. D. Khakhaev, Opt. Spektrosk. **48**, 457 (1980) [Opt. Spectros. USSR **48**, 251 (1980)].
[9] A. A. Mityureva and N. P. Penkin, Opt. Spektrosk. **66**, 1220 (1989) [Opt. Spectros. USSR **66**, 710 (1989)].
[10] D. A. Rall, F. A. Sharpton, M. B. Schulman, L. W. Anderson, J. E. Lawler, and C. C. Lin, Phys. Rev. Lett. **62**, 2253 (1989).
[11] R. B. Lockwood, F. A. Sharpton, L. W. Anderson, and C. C. Lin, Phys. Lett. A **166**, 357 (1992).
[12] R. B. Lockwood, L. W. Anderson, and C. C. Lin, Z. Phys. D. **24**, 155 (1992).
[13] M. E. Lagus, J. B. Boffard, L. W. Anderson, and C. C. Lin, Phys. Rev. A **53**, 1505 (1996).
[14] J. O. Phelps and C. C. Lin, Phys. Rev. A **24**, 1299 (1981).
[15] C. C. Lin and L. W. Anderson, Adv. At. Mol. Opt. Phys. **29**, 1 (1991).
[16] R. M. St. John, F. L. Miller, and C. C. Lin, Phys. Rev. **134**, A888 (1964).
[17] J. D. Jobe and R. M. St. John, Phys. Rev. **164**, 117 (1967).
[18] H. R. Moustafa Moussa, F. J. De Heer, and J. Schutten, Physica **40**, 517 (1969).
[19] R. Muller-Fiedler, P. Schlemmer, K. Jung, H. Hotop, and H. Ehrhardt, J. Phys. B **17**, 259 (1984).
[20] W. L. Wiese, M. W. Smith, and B. M. Glennon, *Atomic Transition Probabilities*, Natl. Stand. Ref. Data Ser. Natl. Bur. Stand. No. 4 (U.S. GPO, Washington, D.C., 1966), Vol. I.
[21] C. E. Theodosiou, At. Data Nucl. Data Tables **36**, 99 (1987).
[22] J. O. Phelps, J. E. Solomon, D. F. Korff, C. C. Lin, and E. T. P. Lee, Phys. Rev. A **20**, 1418 (1979).
[23] D. Leep and A. Gallagher, Phys. Rev. A **10**, 1082 (1974).
[24] A. Zajonc and A. Gallagher, Phys. Rev. A **20**, 1393 (1979).
[25] S. Chung (private communications).
[26] M. Inokuti, Rev. Mod. Phys. **43**, 297 (1971).
[27] N. F. Mott and H. S. W. Massey, *The Theory of Atomic Collisions*, 3rd ed. (Oxford University Press, London, 1965).
[28] W. L. Wiese, M. W. Smith, and B. M. Miles, *Atomic Transition Probabilities*, Natl. Stand. Ref. Data Ser., Natl. Bur. Stand. No. 22 (U.S. GPO, Washington, D.C., 1969), Vol. II.
[29] K. T. Chung and R. P. Hurst, Phys. Rev. **152**, 35 (1966).
[30] A. Dalgarno and R. M. Pengelly, Proc. Phys. Soc. London **89**, 503 (1966).
[31] I. I. Fabrikant, J. Phys. B **19**, 1527 (1986).